

# TMS MI-BCI in the Source Space

Alexandra Mikhael, Arman Paydarfar, Geffen Cooper

**Abstract**—This study investigates the effects of inhibitory 1 Hz repetitive transcranial magnetic stimulation (rTMS) on motor imagery (MI) performance and brain-computer interface (BCI) decoding, using source-space electroencephalography (EEG) analysis. We employed a two-day experimental protocol involving three participants, combining MI tasks with EEG recording before and after rTMS over the motor cortex. A Riemannian geometry-based BCI decoding pipeline was used, incorporating adaptive recentering for online unsupervised domain adaptation. Time-frequency and source localization analyses revealed a spatial shift in event-related desynchronization (ERD) from the contralateral motor cortex to central motor areas following rTMS. Interestingly, BCI decoding performance did not decline after rTMS, and in some cases, showed slight improvement. This may be related to changes in cortical activation patterns, though further study is needed. These preliminary findings indicate that adaptive BCI systems might be able to maintain performance even when brain dynamics are altered, which could have implications for future neurorehabilitation research.

## I. INTRODUCTION

Transcranial Magnetic Stimulation (TMS) has emerged as a powerful tool for modulating neural activity and understanding brain function. When combined with Brain-Computer Interface (BCI) technology, it opens up new possibilities for neurorehabilitation, cognitive enhancement, and neuroplasticity research. In particular, the use of repetitive TMS (rTMS) paired with motor imagery (MI) tasks in a BCI framework offers a promising approach for exploring the neural mechanisms underlying motor control and brain-robot interactions.

Repetitive Transcranial Magnetic Stimulation (rTMS) at 1 Hz has been widely studied for its *inhibitory* effects on cortical excitability. When applied over motor regions, 1 Hz rTMS has been shown to reduce the excitability of the underlying neural circuits, which is thought to reflect a form of synaptic depression [1], [2]. This inhibitory modulation can have a significant impact on motor imagery tasks, which rely on the activation of motor-related brain areas. The ability to reduce cortical excitability in these regions through 1 Hz rTMS could enhance the specificity and effectiveness of motor imagery training by potentially inducing a more controlled and precise neural activation pattern.

In the context of motor imagery, where individuals imagine movements without physical execution, the inhibitory effects of 1 Hz rTMS may help to ‘fine-tune’ the motor system, making it more receptive to voluntary motor control and improving the brain’s response to subsequent motor tasks [3]. Moreover, rTMS can be used as a neuromodulatory tool to induce neuroplastic changes, potentially aiding in recovery from motor impairments such as those seen in stroke or other neurological disorders [4]. For example, in [5] 1 Hz rTMS was

applied to the contralesional hemisphere to reduce its excessive activity. This helped to increase excitability and activity in the ipsilesional motor cortex. When paired with brain-computer interface (BCI) training, this approach led to significant improvements in motor function, demonstrating the combined benefits of inhibitory rTMS and targeted neurorehabilitation.

This study aims to explore the effects of rTMS on motor imagery tasks by employing source-space EEG to assess how inhibitory 1 Hz rTMS modulates brain activity in real-time. By utilizing source-space analyses, the project seeks to examine how neural activity shifts within motor-related brain areas, offering insights into the underlying mechanisms of motor imagery and the potential impact of TMS on motor cortex plasticity. Additionally, by pairing rTMS with a BCI, this project will investigate the feasibility of using this combined approach for applications in motor rehabilitation and neurofeedback

## II. METHODS

This section describes the signal processing pipeline and machine learning implementation. Before addressing these components, we will first provide an overview of the experimental setup and design developed (Section II-A).

### A. Experimental Setup

In this project, the experimental paradigm shown in Figure 1 was designed to investigate the effects of 1Hz rTMS on motor imagery and BCI performance.

Three subjects participated in this experiment, equipped with a 64-channel EEG cap. On the first day, rTMS was not used. This session was done as BCI calibration and Online BCI sessions. On the second day, there was detection of the location of the motor hotspot and the stimulation threshold. During this phase, single pulse TMS was applied over the motor cortex to find the hotspot that would give a right hand movement, as well as the intensity threshold where an EMG signal was detected.

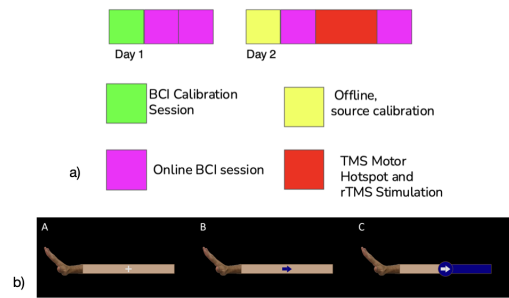


Fig. 1: a) Experimental Protocol, b) Visual Interface

During the offline and online sessions, subjects were asked to perform motor imagery of the right hand. They were seated in a chair with a right arm rest, neck, and cheek rest, in front of a laptop where the task was shown. The screen displayed a central fixation in the middle of a bar, with a hand on the left, as shown in Figure 1. During the trial, an arrow appeared in the middle of the bar in blue and to the right to indicate that it is a rest trial and in red to the left to indicate that it is a MI trial.

For the offline sessions, the bar would fill up continuously for the trial time and the participant asked to rest or perform MI during the whole time. For the online sessions, the bar would fill up depending on the subject's modulation of brain activity, and the trial would be completed if the threshold was reached, indicated by a vertical line in the bar.

### B. Signal Processing

The data was acquired using the LOOP software developed by the Clinical Neuroprosthesis and Brain Interfaces Lab, with an antNeuro64 amplifier [6] operating at a sampling rate of 512 Hz. The first 64 channels were designated for EEG data, with channel 69 used as the trigger channel, as per the instructions. Channels M1, M2, and EOG were excluded.

Prior to feature extraction, EEG signals were preprocessed to enhance signal quality and suppress physiological and environmental artifacts. Signals were bandpass filtered between 8–12 Hz using a second-order Butterworth filter to isolate the mu rhythm, which is most closely associated with motor imagery (MI) activity [7]. In addition, a 60 Hz notch filter was applied to attenuate line noise contamination from electrical sources.

For physiological signal analysis, a surface Laplacian filter was employed to spatially sharpen the EEG data and improve localization of sensorimotor cortical activity. However, for the machine learning pipeline based on covariance matrices, Laplacian filtering was not applied. Instead, raw bandpass-filtered signals were directly used to preserve the spatial covariance structure critical for Riemannian-based classification [8].

Following preprocessing, the EEG data were segmented into overlapping 0.5-second windows with a 1/16th second step size to generate temporal samples for subsequent covariance matrix computation.

### C. ERD/ERS Time-Frequency Analysis

First, EEG data and Marker values were extracted from the .gdf files. The following 27 EEG channels were selected for feature extraction: FP1, FP2, F7, F3, FZ, F4, F8, FC5, FC1, FC2, FC6, T7, C3, CZ, C4, T8, CP5, CP1, CP2, CP6, P7, P3, PZ, P4, P8, O1, OZ, and O2. These channels primarily cover the frontal, central, parietal, and occipital regions, with a strong emphasis on the sensorimotor cortex—the area most relevant to motor imagery tasks [7]. A notch filter at 60 Hz was applied to the raw data to remove line noise. Subsequently, the EEG data was filtered using a bandpass filter from 8 to 30 Hz. Epochs were extracted using the

marker values and grouped by task : rest vs MI epochs.

To analyze brain dynamics during motor imagery (MI) and rest (REST), we computed and visualized Event-Related Desynchronization (ERD) and Synchronization (ERS) topographic maps based on EEG recordings. A baseline period was defined from -1 to 0 seconds relative to event onset, and data were analyzed in the 0 to 5 seconds post-event interval. Time-frequency representations (TFRs) were computed using the multitaper method for both conditions, and baseline correction was applied using a log-ratio method to highlight relative changes in power. The results were averaged across trials to obtain condition-specific TFRs. To ensure consistent visualization, a common color scale was established based on the 2nd and 98th percentiles of the combined ERD/ERS values. Topographic maps were then plotted across sliding 0.5-second windows to illustrate the spatial and temporal evolution of ERD/ERS patterns over the scalp.

### D. Source Space Analysis

In this analysis, we aimed to perform source-level localization and quantification of ERD/ERS patterns associated with MI and rest (REST) conditions. First, we computed the noise covariance matrix using the baseline period from -1.0 to 0.0 s with a shrinkage estimator to regularize the covariance structure, which improves the robustness of inverse solutions, especially with limited data.

The anatomical model was based on the 'fsaverage' template subject provided by MNE, where a source space with oct6 spacing (approximately 5 mm between sources) was created to discretize the cortical surface. A realistic 3-layer Boundary Element Model (BEM) was generated to model the conductive properties of the scalp, skull, and brain tissues, and a forward model was computed to map neural currents to scalp EEG potentials. The coregistration transformation was assumed to be 'fsaverage', matching the template's montage and MRI. during motor imagery tasks.

We constructed the inverse operator using the weighted minimum norm estimate (wMNE) approach, incorporating both depth weighting and orientation constraints (loose=0.2, depth=0.8) to obtain spatially distributed source estimates with a bias towards superficial sources corrected. Using this inverse operator, we applied source reconstruction to the epoched EEG data separately for the MI (marker '9') and REST (marker '5') conditions. For each condition, source power was computed by squaring the source estimates and averaging over time and trials. We then calculated ERD/ERS maps by taking the logarithmic ratio (in dB scale) between the MI and REST conditions, providing a quantitative measure of cortical activation changes.

To visualize the ERD/ERS maps, we created a SourceEstimate object representing the spatial distribution of ERD/ERS values across the cortical mesh. Anatomical parcellations were loaded from the 'aparc' atlas, and regional

source signals were extracted by averaging within each anatomical label, allowing us to summarize ERD/ERS at the brain parcel level. We plotted these results using bar graphs, showing ERD/ERS for each brain region.

Furthermore, dynamic spatiotemporal evolution of motor imagery activity was visualized by averaging the source time courses across trials and creating an animated 3D brain movie, which was saved for further inspection. Cortical surface plots with color maps encoding ERD (desynchronization) and ERS (synchronization) effects were generated, enhancing interpretability of the spatial patterns. Color scaling and colormaps were chosen to distinctly visualize increases and decreases in oscillatory power. Overall, this source localization pipeline allowed for a detailed characterization of the spatial distribution and magnitude of cortical activity changes during motor imagery, supporting a mechanistic understanding of the brain's motor networks in this experimental paradigm.

#### E. Feature Extraction

Channels used were as described in Section II-C. Focusing on this subset improves the signal-to-noise ratio, reduces irrelevant input from non-task-related areas, and lowers the dimensionality of the covariance matrices, enhancing numerical stability for subsequent Riemannian processing.

We extracted spatio-spectral features from EEG signals using sample-wise covariance matrices, which effectively capture the neural patterns associated with motor imagery (MI). Covariance-based representations are widely employed in MI-BCI systems, either directly as features or as inputs to spatial filter learning [9].

First, EEG signals were bandpass filtered between 8–30 Hz using a second-order Butterworth filter to isolate the relevant MI-related frequency bands [7]. The filtered signals were then segmented into overlapping 0.5-second windows with a step size of 1/16th of a second to generate temporal samples.

Each sample, denoted as  $\mathbf{X} \in \mathbb{R}^{C \times T}$  with  $C$  channels and  $T$  time points, was used to calculate a trace-normalized sample covariance matrix.

$$\mathbf{C} = \frac{\mathbf{XX}^\top}{\text{Tr}(\mathbf{XX}^\top)} \quad (1)$$

Trace normalization ensures scale invariance across samples [8]. These matrices, which are symmetric and positive semi-definite by construction, are regularized using a shrinkage estimator to guarantee positive definiteness, thus making them suitable for operations on the Riemannian manifold of symmetric positive definite (SPD) matrices.

When estimating covariance matrices, we initially employed the Ledoit-Wolf shrinkage method [10] to enhance numerical stability, particularly under conditions where the number of samples was limited relative to the number of EEG channels. The Ledoit-Wolf approach automatically estimates an optimal shrinkage coefficient, making it attractive for high-dimensional, low-sample-size problems.

However, in practice, we observed that automatic shrinkage occasionally led to inconsistent performance across sessions

and subjects. Therefore, we adopted a manually tuned basic shrinkage approach as described in the scikit-learn documentation [11]. In this method, the empirical covariance matrix  $\mathbf{S}$  is convexly combined with a scaled identity matrix to obtain the shrunk covariance estimate:

$$\mathbf{S}_{\text{shrunk}} = (1 - \alpha)\mathbf{S} + \alpha\mu\mathbf{I} \quad (2)$$

where  $\alpha \in [0, 1]$  is the shrinkage intensity,  $\mu = \frac{1}{p}\text{tr}(\mathbf{S})$  is the average variance,  $p$  is the number of channels, and  $\mathbf{I}$  is the identity matrix. By manually adjusting  $\alpha$ , we achieved more stable and consistent model performance across calibration sessions. The shrinkage parameters used for the subjects described in this manuscript range between 0.1 and 0.3.

#### F. Riemannian Geometry Framework and Adaptive Recentering

In our BCI decoding pipeline, we adopt the Riemannian geometry framework to model EEG covariance matrices as points on the manifold of symmetric positive definite (SPD) matrices [8]. This approach enables geometric operations such as distance and averaging to be performed in a way that respects the intrinsic structure of the data.

Given a sample covariance matrix  $\mathbf{C}$  computed from a windowed EEG segment, classification is performed using a Minimum Distance to Mean (MDM) classifier [12], which assigns each sample to the class whose Riemannian mean  $\tilde{\mathbf{C}}_k$  is closest under the affine-invariant Riemannian metric (AIRM):

$$\delta_R(\mathbf{C}_1, \mathbf{C}_2) = \left\| \log \left( \mathbf{C}_1^{-1/2} \mathbf{C}_2 \mathbf{C}_1^{-1/2} \right) \right\|_F \quad (3)$$

To address inter-subject and intra-subject variability, we apply a recentering transform that shifts the covariance distribution of incoming samples toward the identity matrix, effectively whitening the data. This is implemented via the affine-invariant transformation:

$$\tilde{\mathbf{C}} = \mathbf{T}^{-1/2} \mathbf{C} \mathbf{T}^{-1/2} \quad (4)$$

where  $\mathbf{T}$  is the current recentering matrix.

*a) Geodesic Interpolation.:* To adapt the recentering matrix  $\mathbf{T}$  over time, we use geodesic interpolation between the previous recentering matrix  $\mathbf{T}_{i-1}$  and the incoming sample covariance  $\mathbf{C}_i$  [?]. The geodesic between two SPD matrices is given by:

$$\gamma(\mathbf{C}_1, \mathbf{C}_2, t) = \mathbf{C}_1^{1/2} \left( \mathbf{C}_1^{-1/2} \mathbf{C}_2 \mathbf{C}_1^{-1/2} \right)^t \mathbf{C}_1^{1/2}, \quad t \in [0, 1] \quad (5)$$

The incremental update of the recentering matrix at each step is:

$$\mathbf{T}_i = \begin{cases} \mathbf{C}_1, & i = 1 \\ \gamma(\mathbf{T}_{i-1}, \mathbf{C}_i, \frac{1}{i+1}), & i > 1 \end{cases} \quad (6)$$

This update progressively incorporates information from new samples, improving alignment between the test and training distributions while remaining on the manifold [13].

The recentered covariance is then computed as:

$$\tilde{\mathbf{C}}_i = \mathbf{T}_i^{-1/2} \mathbf{C}_i \mathbf{T}_i^{-1/2} \quad (7)$$

Following recentering, the sample  $\tilde{\mathbf{C}}_i$  is classified using the MDM decoder trained on expert data.

During online sessions, only the recentering matrix  $\mathbf{T}_i$  is adapted incrementally, while the class prototypes  $\bar{\mathbf{C}}_k$  remain fixed. The recentering transformation shifts each incoming covariance matrix closer to the original training distribution, mitigating covariate shift caused by subject variability and session drift. This process enables fully unsupervised domain adaptation between expert and naïve users without requiring labeled online data [14], [15].

By performing online unsupervised adaptation solely through incremental recentering, our framework reduces non-stationarity, maintains alignment with the training distribution, and supports stable real-time decoding without the need for extensive subject-specific recalibration.

### III. RESULTS

#### A. ERD/ERS Time-Frequency Plots

We used this time-frequency analysis to investigate the effects of rTMS on the typical ERD/ERS seen during MI – ERD over the motor cortex contralateral to the target hand. For that, we compared the topoplots during online sessions pre- and post-rTMS as shown in Figure 2. As you can see, we observe the typical ERD over the left motor cortex during offline and online sessions pre-rTMS. However, an interesting observation was the fact that this ERD location shifted to a more central brain region post-rTMS. And this was also seen for subject 205.

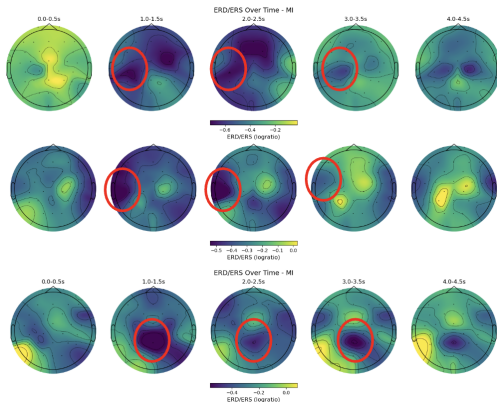


Fig. 2: ERD/ERS Time-Frequency Analysis topoplots for subject 202. First row is for offline session data, second row is for online session pre-rTMS and last row is for online session post-rTMS data.

#### B. Source Space Analysis

In order to better quantify and visualize this shift in ERD localization, we performed a source space analysis on the data pre- vs post-rTMS. We observed similar results : rTMS induced inhibition of activity in the targeted region seen by the disappearance of the ERD over the left motor cortex compared

to pre-rTMS. A new ERD was localized over the central region, indicating that the brain is trying to recruit central motor regions to be able to perform MI, since the usual motor area involved has been inhibited.

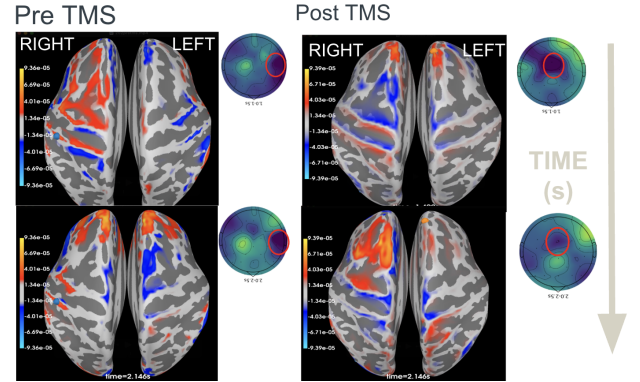


Fig. 3: Source Space Analysis topoplots for subject 202.

#### C. Model Architecture

We employed a Riemannian geometry-based classification framework to decode motor imagery (MI) tasks from EEG signals. Covariance matrices were computed from 0.5-second sliding windows (step size: 1/16th second) and trace-normalized to ensure scale invariance. To mitigate intersession and intersubject variability, we applied online adaptive recentering via geodesic interpolation toward the identity matrix. In the Personally Adjusted Recentering (PAR) framework, the class prototypes were additionally updated by supervised geodesic interpolation with a small learning rate ( $\eta = 0.001$ ). Classification was performed using a Minimum Distance to Mean (MDM) classifier on the Riemannian manifold of symmetric positive definite matrices.

#### D. K-Fold Cross-Validation Accuracy

We evaluated model performance during the initial calibration sessions using K-fold cross-validation. The number of samples collected for Rest and MI conditions, as well as the cross-validated decoding accuracies, are summarized in Table I.

TABLE I: K-fold Cross-Validation Results During Calibration

Subject	Calibration Session	Sample Size (Rest/MI)	K-Fold Accuracy
202	1	40/40	69%
202	2	30/30	77%
205	1	40/40	62%
205	2	30/30	62%

The results indicate that the model achieved reliable above-chance decoding across subjects and sessions, with accuracies ranging from 62% to 77%.

#### E. Pseudo-Online Analysis

We evaluate our trained model using a pseudo-online approach. This consists of applying the trained MDM decoder to the EEG data collected during the *online* sessions. As shown

in Figure 1, there are three online BCI sessions, one on day 1, and two (before and after TMS) on day 2. The first online session consists of 4 runs while the second and third online sessions consist of 3 runs each. A given run has 20 trials evenly split between the rest class and the motor imagery of the right arm (MI) class. The duration of an online trial depends on the real-time decoder used during data collection. The decoder outputted a prediction, stopping the trial, when sufficient evidence was gathered. Otherwise, the trial times out if no prediction is made after seven seconds. The purpose of the pseudo-online analysis is to simulate how our trained decoder would perform when applied in a real-time setting rather than an offline setting.

For each trial, we first preprocess the raw EEG data using notch and bandpass filtering as described in section II-E. In addition, we apply a baseline correction by subtracting the mean value of a one second window of raw EEG data *before* the trial start.

Then, as described in section II-E we segment the data into 0.5-second windows with a 1/16th of a second overlap and extract the covariance matrices of the filtered EEG signals as features. Following section II-F, we apply adaptive recentering to whiten the data in an online fashion.

Given the recentered features for a given window, we apply the MDM decoder which outputs a probability for each class (rest and MI). Recentering and feature extraction is repeated for each window in a given trial such that a trace of probabilities is obtained for each trial. In Figure 4, we show an example of the decoder output for a specific trial. The probability output of the decoder for each window is plotted over time. To obtain the final class prediction, we choose the class with the highest average probability (dashed lines) over the whole trial. In this plot, the rest class is predicted.

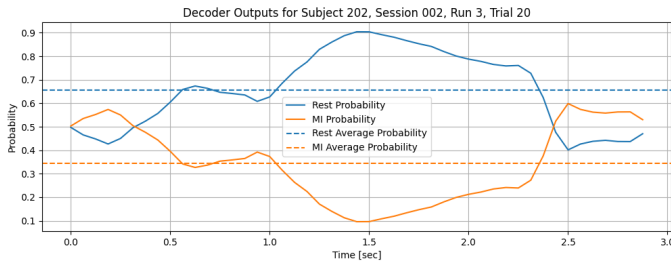


Fig. 4: Decoder outputs for a specific trial. The *solid* blue and orange lines show the class probabilities for the rest and MI classes respectively for each window. The start time of each window is shown on the x-axis. The *dashed* blue and orange lines show the *average* probability across all windows in a trial and are used to make the final prediction.

#### F. Pseudo-Online Evaluation

To evaluate the MDM-decoder, we apply the pseudo-online analysis procedure outlined above to every trial in the three online sessions. For the evaluation metrics, we use the True Positive Rate (TPR) and True Negative Rate (TNR) as defined in Equation 8. We define a True Positive (TP) as a *hit* for the MI class and a True Negative (TN) as a *hit* for the rest class. We define a False Negative (FN) as a *miss* or *timeout*

during the MI class trial and a False Positive (FP) as a *miss* or *timeout* during the rest class trial. These metrics measure how well *each* class is being identified.

$$TPR = \frac{TP}{TP + FN}, \quad TNR = \frac{TN}{TN + FP} \quad (8)$$

We plot the TPR and TNR in Figures 5 and 6 respectively. In each plot, the left panel shows the results for the real time algorithm applied during data collection while the right panel show the results of our pseudo online analysis. For both the real time and pseudo online analysis, the TPR (Figure 5) of *both* subjects increases when comparing the pre-TMS and post-TMS sessions. This means that the hit rate for the MI class increases between the pre-TMS and post-TMS sessions. This trend is interesting given the expected and observed (Figure 2) inhibitory effects of 1 Hz rTMS.

The trend for the TNR is less conclusive. Subject 205 shows an increase in the hit rate of the rest class for both the real time and pseudo online sessions types while the TNR for subject 202 seems to decrease for the pseudo online analysis.

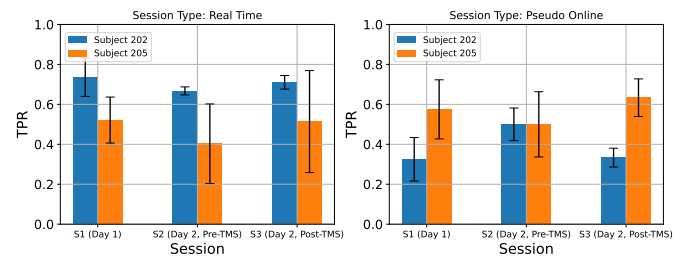


Fig. 5: The True Positive Rate in the real time (left) and pseudo online (right) sessions. The blue and orange bars show the average TPR (across runs) for subject 202 and 205 respectively while the black bars show the standard deviation (across runs). The real time session shows the results for the algorithm applied during data collection while the pseudo online session shows our results.

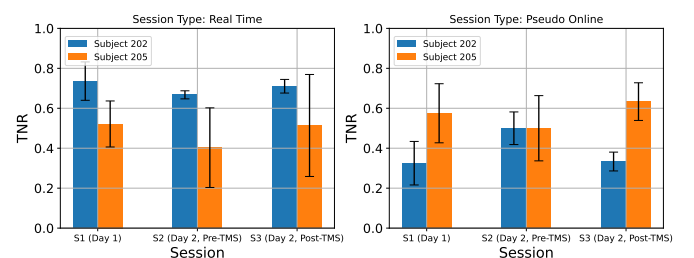


Fig. 6: The True Negative Rate in the real time (left) and pseudo online (right) sessions. The blue and orange bars show the average TNR (across runs) for subject 202 and 205 respectively while the black bars show the standard deviation (across runs). The real time session shows the results for the algorithm applied during data collection while the pseudo online session shows our results.

#### G. Statistical Analysis

To more rigorously analyze the trend of the TPR and TNR across the online sessions, we use a t-test to determine if there

is any statistically significant difference in the BCI decoding performance before and after applying TMS.

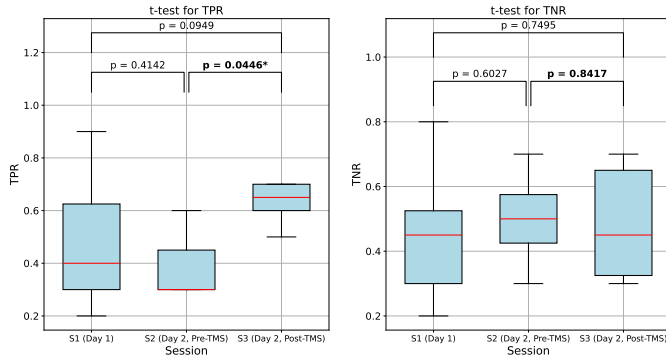


Fig. 7: Box plots and t-tests for the TPR (left) and TNR (right) between online sessions (over all runs of both subjects). Each box ranges from the first quartile to the third quartile of the data and has a red line at the median. The whiskers range from the box to the farthest data point lying within 1.5 times the inter-quartile range from the box. Since session one has a different number of runs compared to sessions two and three, we use an *unpaired* t-test to compare as shown by the *unbolded* p-values. To compare sessions two and three (before and after TMS), we use a paired t-test as shown by the **bolded** p-values. A star shows a statistically significant result ( $p < 0.05$ ).

Figure 7 shows box plots and t-tests for each online session for the pseudo-online setting. We compare every session against each other, using an unpaired t-test to compare against session one since it has a different number of runs. For the TPR, we see that there is a statistically significant improvement in the BCI decoding result when comparing session 2 (pre-TMS) and session 3 (post-TMS). However, it is difficult to conclude whether this results from TMS or it is a result of practicing motor imagery. We note that session two has a lower TPR compared to session one even though there were no notable changes in the experimental setup. We also note that the improvement between session three and session one is not statistically significant. Thus, we *cannot* conclude that the statistically significant improvement between session two and session three was due to TMS. For the TNR, we observe no trend or statistically significant result, reflecting that the ability of the decoder to detect the rest state did not change between sessions.

#### IV. DISCUSSION

Despite the observed spatial shift in ERD/ERS localization following inhibitory rTMS, both the real-time and pseudo-online decoder performances were not impaired; rather, decoding accuracies slightly improved post-rTMS.

One plausible explanation is that the rTMS-induced reorganization led to a more spatially focused or coherent activation pattern over central motor regions. This could have enhanced the discriminability between Motor Imagery (MI) and Rest conditions at the level of the EEG covariance structure, benefiting the Riemannian decoder. In particular, the adaptive recentering framework may have helped accommodate the

shift by aligning incoming covariance matrices toward the new post-rTMS distribution without requiring explicit retraining.

Moreover, inhibitory rTMS may have suppressed maladaptive or noisy cortical activity in surrounding motor or premotor regions, thereby improving the signal-to-noise ratio of MI-related modulations. This could explain why classification performance did not deteriorate, even though the spatial signature of ERD shifted.

Together, these findings suggest that inhibitory rTMS can modulate cortical dynamics without necessarily impairing BCI decoding—and that adaptive recentering methods can robustly handle physiological reorganization during real-time operation.

#### A. Limitations

It is important to note that the present study was conducted with only two subjects and a limited number of recording sessions. Consequently, the findings should be interpreted as preliminary observations rather than definitive conclusions. The absence of a larger statistical dataset precludes rigorous statistical testing and limits the generalizability of the results. Future studies with a greater number of participants and repeated sessions will be necessary to confirm whether the trends observed here are consistent and statistically significant across a broader population.

#### V. CONCLUSION

This study aimed to investigate the effects of inhibitory 1 Hz rTMS on motor imagery (MI) EEG patterns and BCI decoding performance. Based on prior work demonstrating that 1 Hz rTMS reduces cortical excitability, we hypothesized that rTMS would impair MI-related BCI control by disrupting motor cortical activation.

Consistent with our physiological expectations, time-frequency and source space analyses revealed that rTMS induced a spatial shift in ERD/ERS localization, moving activity away from the contralateral motor cortex toward more central regions. However, contrary to our initial hypothesis, both real-time and pseudo-online BCI decoding performance remained stable or slightly improved following rTMS.

We propose that rTMS may have suppressed maladaptive or noisy activity in non-target motor areas, leading to a more coherent or focused cortical activation pattern during MI. Additionally, the use of adaptive recentering methods in our decoding pipeline likely facilitated real-time compensation for shifts in brain dynamics, preserving classification accuracy despite cortical reorganization.

Nonetheless, these findings should be interpreted with caution due to the limited sample size and absence of formal statistical analysis. The study included only two subjects and a restricted number of recording sessions, precluding broad generalization. Future studies involving larger cohorts and repeated sessions will be necessary to determine whether the trends observed here are consistent across individuals and task conditions.

Overall, this work provides preliminary evidence that adaptive BCI systems can maintain, and potentially enhance, performance even under conditions of neuromodulation-induced

cortical reorganization. These results highlight the potential for combining non-invasive brain stimulation and adaptive BCI frameworks to support neuroplasticity and motor rehabilitation applications.

## REFERENCES

- [1] T. Bunse, T. Wobrock, W. Strube, F. Padberg, U. Palm, P. Falkai, and A. Hasan, "Motor cortical excitability assessed by transcranial magnetic stimulation in psychiatric disorders: a systematic review," *Brain stimulation*, vol. 7, no. 2, pp. 158–169, 2014.
- [2] F. Maeda, J. P. Keenan, J. M. Tormos, H. Topka, and A. Pascual-Leone, "Interindividual variability of the modulatory effects of repetitive transcranial magnetic stimulation on cortical excitability," *Experimental brain research*, vol. 133, pp. 425–430, 2000.
- [3] F. Mori, C. Codecà, H. Kusayanagi, F. Monteleone, F. Buttari, S. Fiore, G. Bernardi, G. Koch, and D. Centonze, "Effects of anodal transcranial direct current stimulation on chronic neuropathic pain in patients with multiple sclerosis," *The journal of pain*, vol. 11, no. 5, pp. 436–442, 2010.
- [4] F. C. Hummel and L. G. Cohen, "Non-invasive brain stimulation: a new strategy to improve neurorehabilitation after stroke?," *Lancet Neurology*, vol. 8, pp. 710–718, 2006.
- [5] N. N. Johnson, J. Carey, B. J. Edelman, A. Doud, A. Grande, K. Lakshminarayanan, and B. He, "Combined rtms and virtual reality brain-computer interface training for motor recovery after stroke," *Journal of neural engineering*, vol. 15, no. 1, p. 016009, 2018.
- [6] ant neuro, "Copyright © ant-neuro.com 2024."
- [7] G. Pfurtscheller and F. L. Da Silva, "Event-related eeg/meg synchronization and desynchronization: basic principles," *Clinical neurophysiology*, vol. 110, no. 11, pp. 1842–1857, 1999.
- [8] A. Barachant, S. Bonnet, M. Congedo, and C. Jutten, "Riemannian geometry applied to bci classification," in *International conference on latent variable analysis and signal separation*, pp. 629–636, Springer, 2010.
- [9] B. Blankertz, R. Tomioka, S. Lemm, M. Kawanabe, and K.-R. Muller, "Optimizing spatial filters for robust eeg single-trial analysis," *IEEE Signal processing magazine*, vol. 25, no. 1, pp. 41–56, 2007.
- [10] O. Ledoit and M. Wolf, "A well-conditioned estimator for large-dimensional covariance matrices," *Journal of multivariate analysis*, vol. 88, no. 2, pp. 365–411, 2004.
- [11] F. Pedregosa, G. Varoquaux, A. Gramfort, V. Michel, B. Thirion, O. Grisel, M. Blondel, P. Prettenhofer, R. Weiss, V. Dubourg, J. Vanderplas, A. Passos, D. Cournapeau, M. Brucher, M. Perrot, and Duchesnay, "Scikit-learn: Machine learning in python – covariance estimation," <https://scikit-learn.org/stable/modules/covariance.html>, 2011. Accessed: 2025-04-28.
- [12] A. Barachant, S. Bonnet, M. Congedo, and C. Jutten, "Multiclass brain-computer interface classification by riemannian geometry," *IEEE Transactions on Biomedical Engineering*, vol. 59, no. 4, pp. 920–928, 2011.
- [13] S. Kumar, F. Yger, and F. Lotte, "Towards adaptive classification using riemannian geometry approaches in brain-computer interfaces," in *2019 7th International Winter Conference on Brain-Computer Interface (BCI)*, pp. 1–6, IEEE, 2019.
- [14] P. Zanini, M. Congedo, C. Jutten, S. Said, and Y. Berthoumieu, "Transfer learning: A riemannian geometry framework with applications to brain-computer interfaces," *IEEE Transactions on Biomedical Engineering*, vol. 65, no. 5, pp. 1107–1116, 2017.
- [15] M. Congedo, A. Barachant, and R. Bhatia, "Riemannian geometry for eeg-based brain-computer interfaces; a primer and a review," *Brain-Computer Interfaces*, vol. 4, no. 3, pp. 155–174, 2017.

## VI. CONTRIBUTION STATEMENT

Alex: I implemented the physiological analysis (topoplots) as well as implemented the source space analysis. Arman worked on the decoding, building the model. Geffen worked on the pseudo-online analysis and statistical analysis. We all worked equally on the report and overall for this project !

Arman: I implemented the Reimannian Decoder with adaptive re centering and explained that portion for the report in the methods section. Alex worked on the physiological analysis,

and Geffen utilized the decoder for a pseudo online analysis, he also did the statistical analysis. We all worked equally on the project/report.

Geffen: I applied the trained decoder to the online session data for the pseudo online analysis and obtained the evaluation metrics for statistical analysis. Alex worked on the physiological analysis to generate the topoplots and source space analysis. Arman created and trained the decoder as well as the EEG preprocessing for BCI decoding. We all worked equally on the project and final report.